

The role of austenite twins on variant selection during decomposition in low carbon steels

Ruth Birch^{1*}, Ben Britton¹, Warren J Poole¹

1. Department of Materials Engineering, University of British Columbia, Frank Forward Building, 309-6350 Stores Road, Vancouver, BC, Canada V6T 1Z4

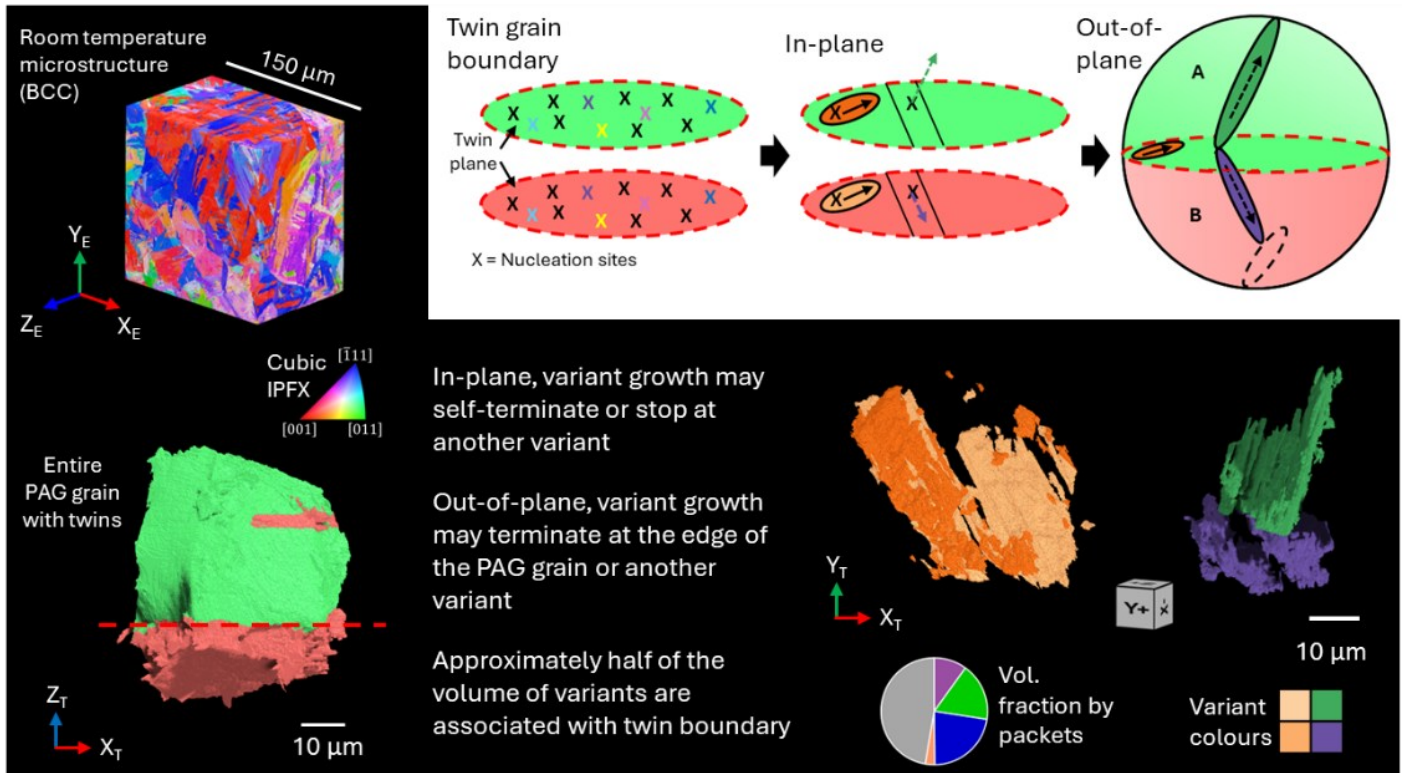
*corresponding author: ruth.birch@ubc.ca

Abstract

Thermomechanical Controlled Processing (TMCP) is widely used to control the microstructure and properties of linepipe or high strength low alloy steels (HSLA). These steels are often joined by welding and used in demanding environments such as the Arctic. In these materials, the thermal path the steel experiences is critical for understanding microstructural evolution during processing. A key step is the solid-state phase transformation during cooling from the high-temperature austenite to the room-temperature microstructure which significantly influences the final mechanical properties. Specifically, the population of different variants and grain shapes that form affect the types and morphology of the grains, and grain boundary network which influence strength and toughness of the final component. In this paper, we apply 3D microscopy using a Xe-plasma focussed ion beam scanning electron microscope (pFIB-SEM) which is equipped with electron backscatter diffraction (EBSD) in a static configuration to characterize the room temperature microstructure of a steel sample, and then use a '2.5D' prior austenite grain (PAG) reconstruction code to explore the relationship between the austenite phase and the room temperature microstructure. A significant result for the present work is the collection, and analysis, of data from a large volume ($150 \times 150 \times 100 \mu\text{m}^3$, with a $(200 \text{ nm})^3$ voxel size) which enables analysis of a complete prior austenite grain. Analysis of variants within this grain demonstrates that high-temperature twin boundaries likely govern variant selection and grain growth in the child microstructure. This suggests opportunities to engineer novel microstructures by controlling the high-temperature grain boundary character.

Keywords (keywords list): 3D EBSD, Steel, Twin grain boundary, variant selection

Graphical abstract



1 Introduction

Thermomechanical Controlled Processing (TMCP) is widely used to control the microstructure and properties of linepipe and high strength low alloy (HSLA) steels. Further, these steels are often joined using high energy welding processing (e.g. gas metal arc or submerged arc welding) and used in demanding environments such as the Arctic where low temperature toughness is a critical property. The potential exists to tailor the mechanical properties of the steel to the application if one had an improved understanding of the microstructural evolution at each step. For these steels, a key step is the solid-state phase transformation during cooling from the high-temperature austenite phase to the room-temperature microstructure, in particular, at high cooling rates found in welding or during accelerated cooling after hot rolling. Here, complex bainitic or martensitic microstructures [1], are produced which significantly influence the final mechanical properties. Specifically, the population of different variants and grain shapes that form affect the types and morphology of the grains, and the grain boundary network which influences the strength and toughness of the final component [2]. Certain boundary types may have a specific influence on variant selection (e.g. high angle, low angle or special boundaries such as annealing twins) [3]. With the availability of three-dimensional electron backscatter diffraction (3D EBSD) experiments, we can now look at variant selection in complete prior austenite grains.

The high temperature, austenite microstructure, whilst difficult to observe directly, can be reconstructed from the final, room temperature bainitic or martensitic microstructure using the orientation relationship (OR) between the two phases. Common ORs used for steel are Kurdjumov-Sachs (KS) where $(111)_\gamma // (011)_\alpha$ and $[\bar{1}01]_\gamma // [\bar{1}\bar{1}1]_\alpha$, and Nishiyama-Wasserman (NW) where $(111)_\gamma // (011)_\alpha$ and $[1\bar{1}0]_\gamma // [100]_\alpha$ [4]. Whilst these two ORs are similar, there is a rotation about the closest packed plane, $\{111\}$, of 5.26° [5] and as a result the main difference is that KS gives 24 unique child variants compared with 12 for NW. For any material with a solid-state phase transformation, it is these variants, and the preferential selection of them that can impact the final mechanical properties. For example, less unique variants forming in a prior austenite grain can result in a coarser microstructure, whilst more variants may result in higher local misorientations [3].

Studies of variant selection in steels have included evaluating factors such as the effect of stress [6] or deformation at different points during processing [7] and the effect of prior austenite grain size [8]. Variant selection at grain boundaries has been considered in terms of nucleation rules for parent grain boundaries [9] and it has also been suggested that special grain boundary types, such as twins can play a role.

Annealing twins are a common occurrence in FCC materials with low to medium stacking fault energies [10], including low-carbon steels in the austenite phase field, usually taking the form of a 60° rotation about $\langle 111 \rangle$ (i.e. a $\Sigma 3$ twin) [11] and have been observed forming during austenite grain growth [12]. For the variants, this means that there is a common packet group (variants with the same $[111]$ direction in the parent grain) between the parent grains, which may influence variant selection at the twin boundary. *In situ* experiments using laser scanning confocal microscopy to look at bainite formation have concluded that the presence of twins impacts bainite

growth and morphology [12], and that the twin boundaries can stop bainite growth and provide potential nucleation sites [13].

The presence of twins complicates the reconstruction of the parent phase using EBSD data and reconstruction codes due to the shared packet i.e. there are the same orientations possible for two parent grains. This is important when the OR is strictly obeyed and can be a particular problem if these shared variants are located at the boundary between the grains. In this case, the common variant types can make it very difficult group the data into the correct PAG grain, especially if there is limited angular resolution in the orientation data and/or there is no slight rotation away from the slight PAG-related OR. For more discussion, on twins in reconstruction and methods to address this challenge, see [14].

Whilst most studies are based on 2D metallographic or EBSD observations, with the development of 3D systems, for example, using focused ion beam – scanning electron microscopes (FIB-SEMs) [15–20], research on steels has moved into 3D, opening up opportunities to study grain size and morphology in greater depth.

For example, Petrov et al. [21,22] have used small targeted volumes (e.g. max. $16 \times 14 \times 6 \mu\text{m}^3$ at $0.1 \mu\text{m}^3$ voxel size) to investigate grains and texture in pipeline steels. Parida et al. [23] looked at texture and recrystallisation in modified 9Cr–1Mo steel using two volumes, adapted to the grain size before and after recrystallisation (e.g. area per slice $4 \times 4 \mu\text{m}^2$ vs. $30 \times 10 \mu\text{m}^2$). Mosayebi et al. [24,25] evaluated a triplet of (partial) PAG grains in low carbon martensitic steel, covering a volume of $135 \times 120 \times 75 \mu\text{m}^3$ at $0.5 \mu\text{m}^3$ voxel size for a sample with average PAG grain size of $158.1 \mu\text{m}$. Their analysis includes evaluation of variants and packet groups within the grain, and they observed the 3D arrangement of the packets in a tetrahedral arrangement within the PAG grains and calculated a dominant habit plane of $\{557\}_\gamma$. Finally, Shibata et al. [26] looked at medium carbon steel with a prior austenite grain size of $122 \mu\text{m}$ and fine lath microstructure. They imaged a small volume in 3D, measuring $20 \times 20 \times 6 \mu\text{m}^3$, with a voxel size of $6.25 \times 6.25 \times 5 \text{ nm}^3$, and investigated the local variant configuration by combining the 3D dataset with 2D EBSD and TEM analysis.

In this work, we carried out a 3D EBSD tomography experiment on a linepipe steel to collect a $150 \times 150 \times 100 \mu\text{m}^3$ volume with a fully internal, twinned prior austenite grain, with the aim of evaluating the variants at this twin boundary and the effect on variant distribution within this complete grain.

2 Experimental

2.1 Sample

A linepipe steel with the composition at Table 1 was used for this tomography experiment. The sample was heated to 1150 °C at 50 °C/s with a hold at 1150 °C for 10 mins, then cooled to room temperature at a nominal 50 °C/s (note that the cooling rate slows during the austenite to ferrite transformation). Laser ultrasonic measurements [27] were used to measure an approximate prior austenite grain (PAG) grain size of 40 µm and resulted in a bainitic final microstructure. The sample heat treated was 100 x 11 x 11 mm³. To perform tomography, the sample was sectioned using wire electrical discharge machining (EDM) to approx. 3 x 3 x 5 mm³ to enable the tomography experiment - see supplementary material for more details on geometry.

Table 1 – Composition of line pipe steel used in this work (in wt%).

C	Mn	Cu+Ni+Cr+Mo	V+Nb+Ti
0.06	1.3	<0.9	0.07-0.08

2.2 Tomography

A 3D EBSD tomography experiment was carried out using a TESCAN AMBER X plasma focused ion beam – scanning electron microscope (pFIB-SEM) equipped with an Oxford Instruments symmetry S2 EBSD detector and a TESCAN rocking stage. This instrument has a static EBSD setup, where the sample is facing the EBSD detector, but tilted so that the top of the edge to cut is perpendicular to the FIB beam (see Figure 1). The static setup is described in more detail in [19]. For this experiment, tomography was performed on the sample edge (i.e. no lift out step).

A schematic for the target volume preparation is shown in Figure 1 (A). A 225 x 200 x 15 µm³ (W x L x D) tungsten cap was deposited using a (FIB) voltage of 15 kV and current of 120 nA. Two triangular side trenches were cut to allow the required exit angles and minimise shadowing. These were milled using (FIB) voltage of 30 kV and current of 1 µA – in this case, the chosen region of interest (ROI) was located at the edge of the sample, so one of the trenches is square, as shown in the Figure 1 (A). The sides and front face were then ‘cleaned up’ (polished) using a 30 kV 300 nA polish ready for tomography. An alignment marker was used to align between slices – no post processing alignment was required.

Each slice was cut using a (FIB) voltage of 30 kV and current of 300 nA. The rocking stage y-tilt was used to tilt the sample +6 °/-1 ° during the milling (Figure 1 (C)), with 2 rocking cycles used per cut, again to reduce curtaining artifacts during milling. Imaging and analytics were always collected at y-tilt 0 °.

An EBSD map was captured for each slice using a voltage of 20 kV and a current of 10 nA for an area of 150 x 150 µm² at a step size of 0.2 µm. Patterns were captured at 156 x 128 pixels with an exposure time of 0.5 ms and processed online in Oxford Instruments AZtec software, with a minimum of 6 bands required to index the point.

Each slice took ~12 mins to complete (FIB slicing 5 m 42s, SE Imaging 19 s, EBSD ~5 mins, +overhead). Whilst 700 slices were collected, to address issues at the start and the end of the run, only a subset of 500 slices were used for this analysis. The final analysis volume was $150 \times 150 \times 100 \mu\text{m}^3$ at a voxel size of $(0.2 \mu\text{m})^3$ as shown in Figure 1 (D).

Note that prior to this data set collection, trial experiments were conducted to reduce the risk of FIB-induced damage and ensure that the EBSD data would be collected well. Furthermore, 2D-based EBSD analysis was performed for this steel (and the heat treatment) to ensure that the target volume would have a high likelihood of containing at least one isolated prior austenite grain (i.e. one prior austenite grain/twin set located away from the edges of the volume).

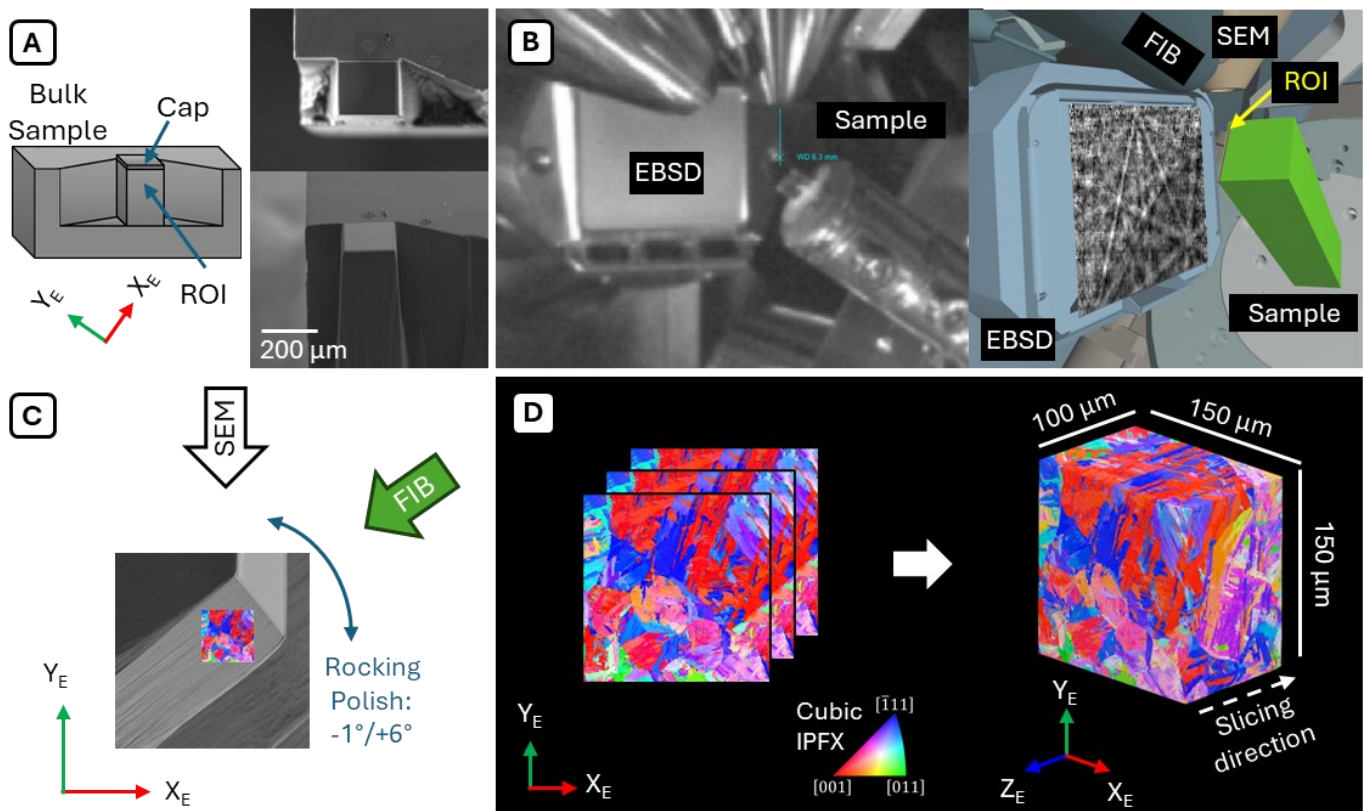


Figure 1 – Tomography overview. (A) Sample Schematic and secondary electron (SE) images at the start of the experiment (Top = FIB – SE; Bottom = SE) Scalebar = 200 μm ; (B) Chamber view and model view of 3D setup; (C) Details of the EBSD map area vs. sample geometry; (D) slices are combined to give the 3D volume – IPFZ.

2.3 Analysis

Data analysis was carried out in MATLAB (2023b & 2024a) using the MTEX toolbox (5.11.2) [28], with visualisation and further analysis in Dragonfly (2024.1 & 2025.1) [29]. Code was developed to routinely exchange data between MTEX and Dragonfly (e.g. to import MTEX-generated EBSD data for visualisation in Dragonfly, and to extract objects from Dragonfly for crystallographic analysis in MTEX).

Prior austenite grain reconstruction was carried out using in house code (3D PAG) which builds on prior work by Nyssönen et al [30] and the authors of this paper [14]. In brief, the 3D PAG code reconstructed each slice in 2D,

including 're-sort' [14] to improve the reconstruction. Subsequently, data in the volume was linked together (using every 10th slice as a seed for naming the parent grains). Then groups of 3 slices were considered at a time to provide a more consistent reconstruction throughout the volume, using a forward and backwards pass approach. Local analysis of the grain considered in this paper was carried out by restricting the problem to the grain region and its immediate neighbours, with an adapted re-sort approach. Note that, to avoid inconsistencies slice to slice, a mean iterative OR was initially calculated (and used throughout) by reconstructing every 10th slice in the volume and averaging the iteratively determined ORs.

The main reconstruction was run using Compute Canada resources, with post processing carried out on a local workstation computer. For the dataset presented, the volume was reconstructed, then a PAG grain was selected, and a secondary check/resort was run on this local grain region to improve the slice to slice reconstruction. When looking at this PAG grain region, to analyse the variants, connected component analysis in Dragonfly was used on each variant in turn, and groups with less than 50 voxels were removed. The output of this was then used for preparing further data analysis using MTEX.

3 Results

A twinned PAG grain pair was isolated from the 3D volume as shown in Figure 2. Cut throughs of the volume showing the grain within the volume, as indicated by the white arrow, is shown in Figure 2 (A) for the initial microstructure and (B) the reconstructed PAG microstructure. The local region to the PAG grain has had the additional processing (a version of ReSort [14] in 3D) to address small issues with the reconstruction – it was not computationally cost effective to expand this to the whole volume at this time. The complete isolated grain is then shown in Figure 2 (C) for the initial microstructure and (D) for the reconstructed microstructure. In all cases, a box representing the full volume is shown to help show the spatial location of the grain. For a 3D video showing the volume and the grain location, see the supplementary material.

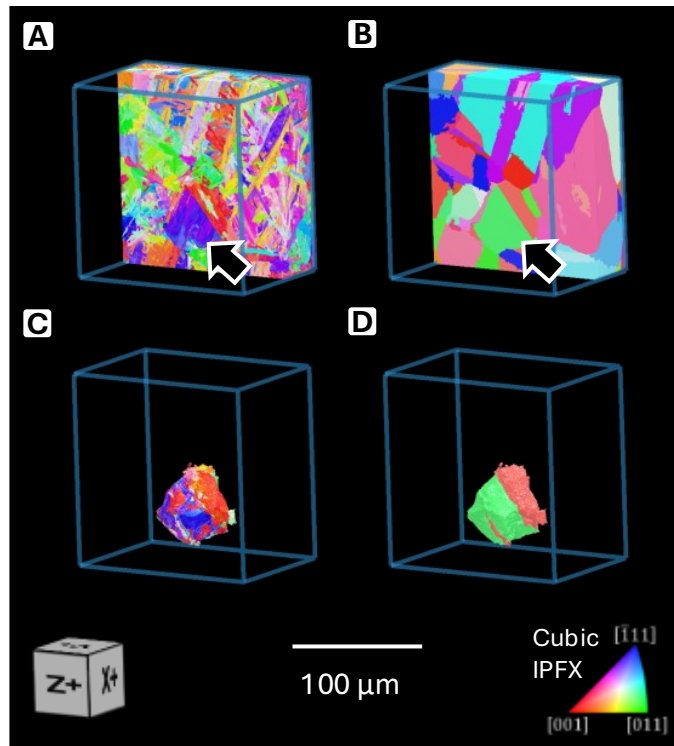


Figure 2 – Cut-throughs showing the location of the isolated grain within the volume. (A) IPFX initial; (B) Reconstructed prior austenite grain (PAG) microstructure with the grain identified with arrows; (C) isolated grain – initial microstructure; (D) isolated grain – reconstructed PAG microstructure. The outline box indicates the full volume.

The isolated grain pair contains a full and a partial twin, both parts with the same parent orientation. The analysis in this paper focusses only on the larger section of the twin, and its boundary, with the smaller twin region excluded from the analysis. The larger grain (green in Figure 2 (D)) and the larger of the twin parts (orange in Figure 2 (D)) will be referred to as PAG A and PAG B, respectively, from this point.

The (rounded) mean grain orientations are (249, 43, 127) for PAG A and (343, 20, 2) for PAG B in the EBSD axis system. The misorientation between the grains is 59.8° about $[\bar{1}11]$. 5-parameter grain boundary analysis was carried out as shown in Figure 3 (A).

To calculate the grain boundary interface normal vector, the grain boundary trace was measured from approximately the centre of the grain pair and the perpendicular bisectors calculated. The grain boundary normal was calculated the intersection of these two zones on the pole figure (Figure 3) and the normal vector was calculated as $[-0.72 \ -0.52 \ 0.34]$ in the sample frame.

Knowledge of this normal vector was used to rotate the crystallographic and spatial microstructure data so that the twin grain boundary plane could be viewed in the (viewing) XY plane. To do this, the data was rotated such that the normal was rotated along the XY zone to the centre of the pole figure and a second rotation was made to align the $[101]_{PAG\ B}$ with the X-axis. The results of this are shown in Figure 3 (B) – original and Figure 3 (C) – rotated with new axis system, along with cubes representing the orientations for the grains in each. For simplicity, the original IPFX colours are used for the grains throughout this paper.

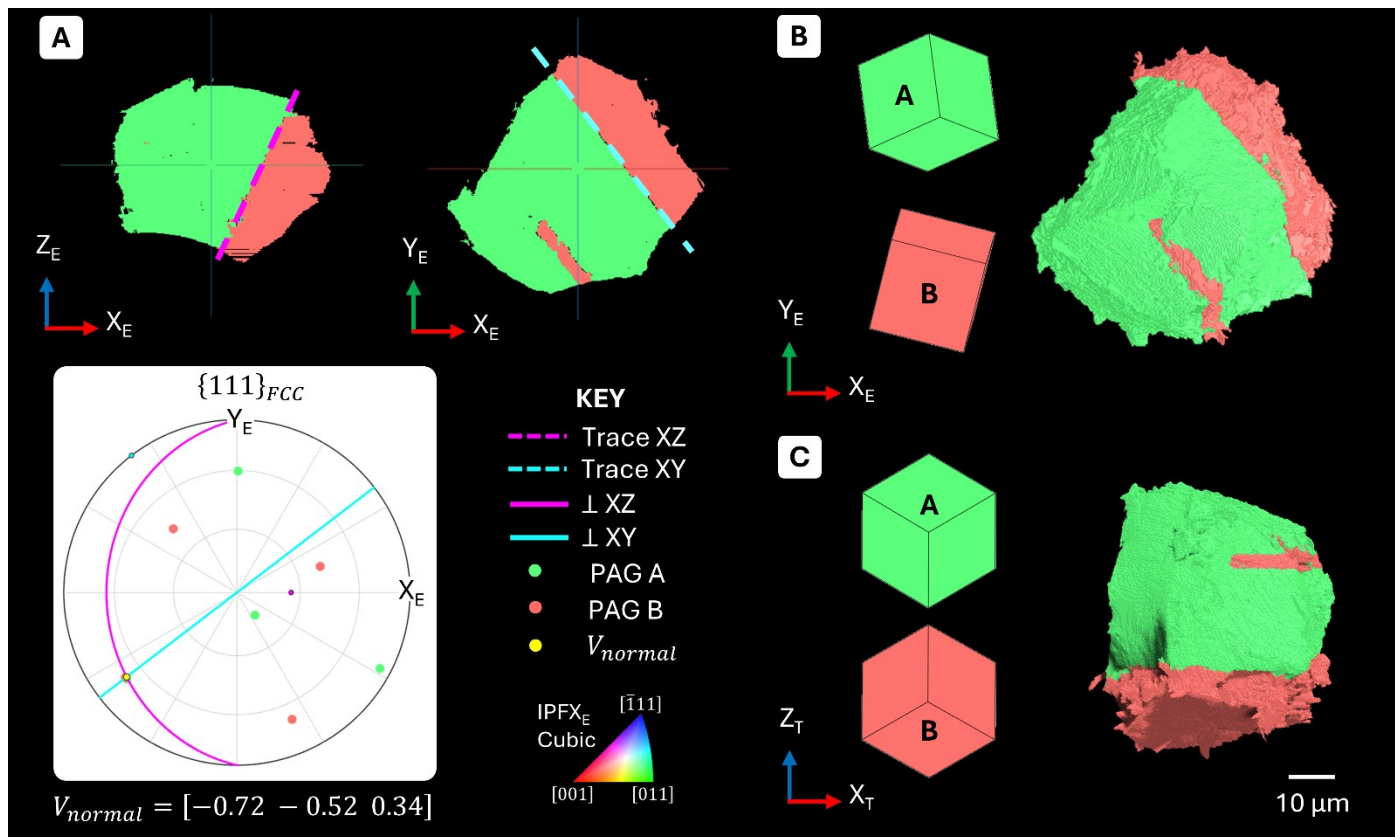


Figure 3 - Isolated twinned grain (A) grain boundary analysis to identify the grain boundary normal – including XZ and XY planes through the centre of the grain with the trace of the grain boundary indicated by the dashed lines and pole figure analysis with the perpendicular bisectors overlaid and grain boundary normal identified; (B) Grain and orientation cubes in the EBSD orientation; (C) Grain and orientation cubes rotated so that the twin plane is the XY plane. IPFX (EBSD orientation) colours used throughout for the grains.

To explore the twin boundary in more detail, a thin region centred on the twin boundary was isolated, as described in the schematic in Figure 4 (A). The region is 2 μm thick, with approximately the same number of voxels belonging to each PAG grain contained within.

Figure 4 (B) shows the experimental results with (i) the complete grain pair, (ii) the thin region, separated by PAG grain association, and (iii) the twin plane at the intersection in both PAG IPF-X colour. The twin boundary is rough, likely due to some local difficulties with assigning points to each parent where the child orientations may belong to either parent grain. This roughness results in ‘gaps’ in the thin region when separated by PAG grain, as highlighted by the blue ellipses in Figure 4 (B-iii) – these are due to the voxels in that region being grouped with the other grain.

The final part of this figure is the twin planes in variant colours (Figure 4 (B-iv)). These are the child orientations grouped into the closest of the 24 variants for each grain, as calculated using the iterative orientation relationship (starting point: Kurdjumov-Sachs). Note that the variant colours can’t be read across between grains. Two observations can immediately be made: (1) the variants in this region are in laths, at approximately 60° from each other, along the $\langle 110 \rangle$ directions in the PAG orientations and (2) there are spatially correlated variants e.g. green in PAG A and purple in PAG B.

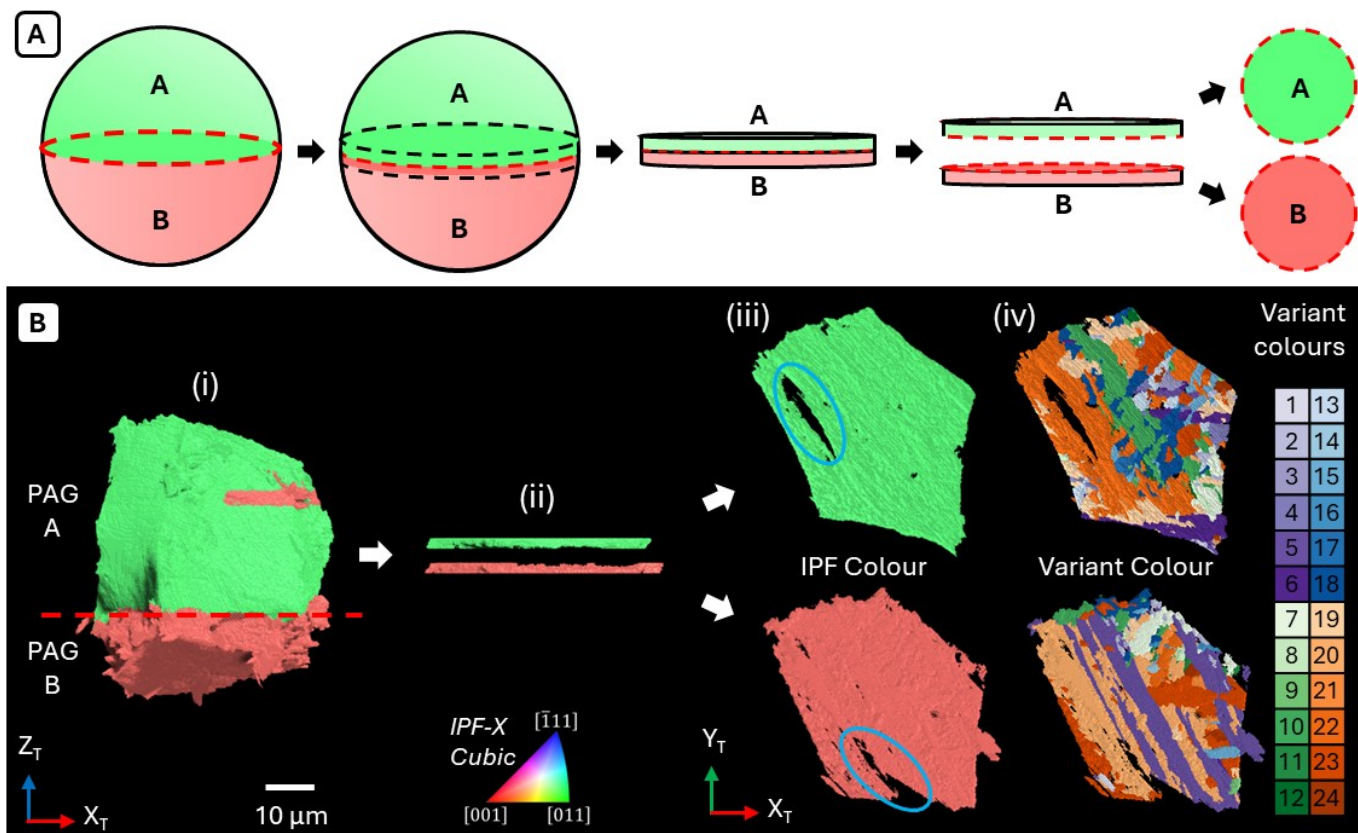


Figure 4 – Twin plane analysis. (A) Schematic showing how a thin region around the twin grain boundary was analysed and the twin planes for each grain shown. (B) Experimental results in IPFX colours for the PAG grains and the twin planes in variant colouring for each PAG grain.

For statistical analysis of the variants, only variants with >50 voxels after connected components 3D (6-connected) analysis in Dragonfly are considered. All 24 variants are found in PAG A, whilst only 21 variants are found in PAG B.

To evaluate the impact of variants found at the twin boundary on the grain as a whole, the distribution of variants was calculated for three regions, in each PAG: (1) the twin boundary region (Figure 4 (B)); (2) variants that intersect with the twin boundary region i.e. the complete (connected) variants that begin/end in the twin boundary region; (3) the complete PAG grain.

An example is shown in Figure 5, using packet groups (where the variants have a common $[111]$ direction in the parent grain) for the variants. Looking at the twin boundary only (Figure 5 (A)), we see that the shared packet group, indicated in orange in both PAG A and PAG B, is dominant in both grains, making up approximately 50% of this region in each case. The shared packet group is due to the twin being a rotation about a $\langle 111 \rangle$ direction, which leads to similar variant orientations in this PAG direction. The minimum misorientation angle between the individual variants in the shared packet is $\sim 5^\circ$ which may lead to some uncertainty in grouping between PAG grains, however it is still clear that this is the dominant packet at the twin boundary for both grains.

Looking at PAG A, as we move into the grain, this proportion changes and other packet groups have higher distributions. In Figure 5 (B), only 3% of the voxels for variants connected to the twin boundary region are associated with the shared packet, indicating that these variants are mostly contained within the twin plane region.

When we consider the whole grain (Figure 5 (C)), the proportion rises slightly to 13%, likely due to voxels within PAG A that are associated with the smaller partial twin grain.

In PAG B, the situation is similar when considering the variants that intersect with the twin boundary region (Figure 5 (B)), we see a reduction in the proportion from 51% to 19%. However, in this smaller grain, this packet group continues to dominate when considering the whole grain.

Looking at the other packet groups, for PAG A, the distribution starts ~equal for the packets, and then two packet groups become dominant (see Figure 5 (A-C)) indicating the growth of some preferred variants. In PAG B, this is more pronounced, with one dominant non-shared packet group (purple) throughout. Both of these results show some preferential nucleation and growth of the variants with respect to packet groups.

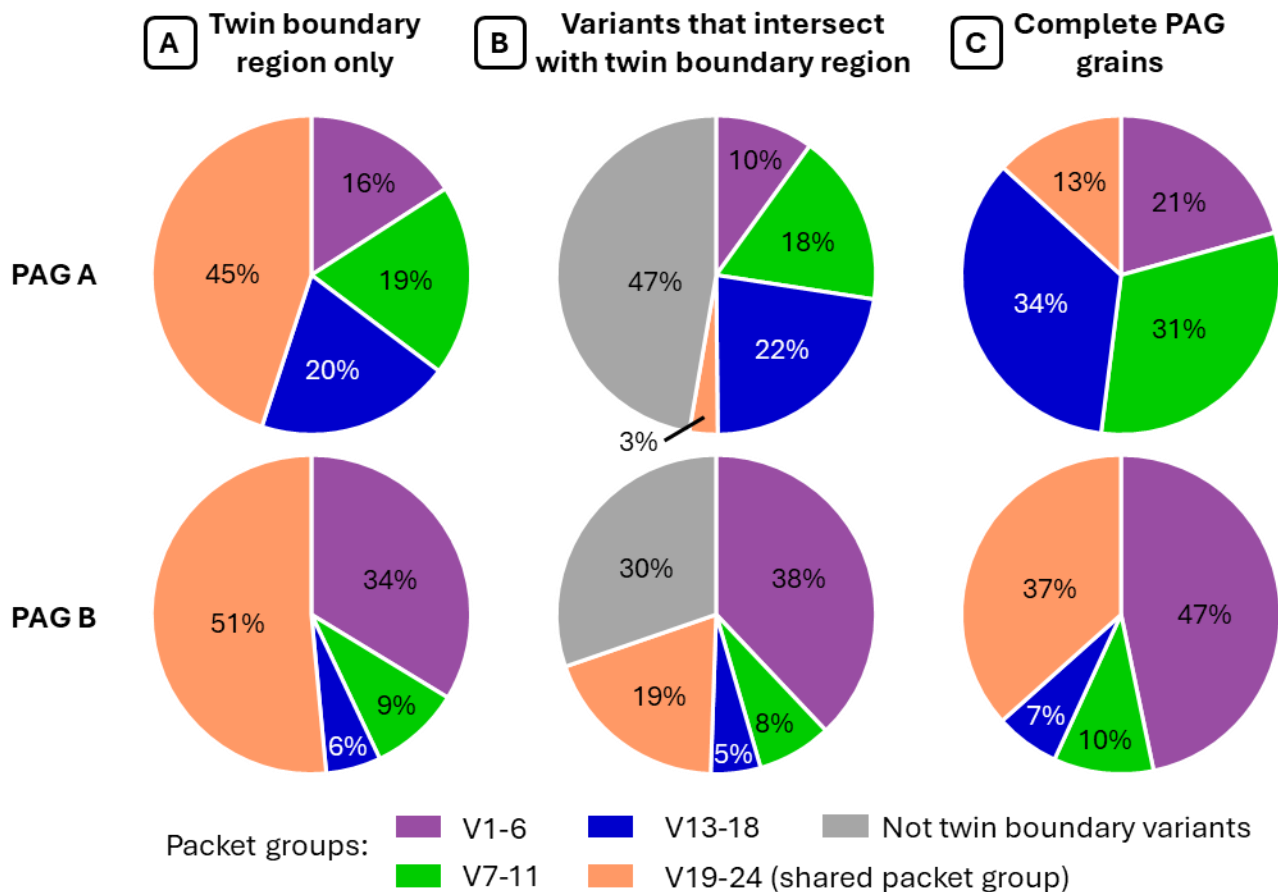


Figure 5 - Variant distribution into packet groups. (A) twin boundary region only – 2 μm box around the twin boundary; (B) variants intersecting with the twin boundary region, including points not associated with the twin boundary; and (C) in the complete PAG grain volume. Variants containing a minimum of 50 voxels included. Total voxels considered: PAG A: 5,192,442 (complete grain) / 176,047 (twin boundary region); PAG B: 1,916,858 (complete grain) / 163,087 (twin boundary region). Variant numbers are specific to the PAG grain – only the shared packet group variants are common (due to symmetry) and can be read across.

Another way to consider the variants is to classify them into terms of Bain groups, where the (001) plane of the variants are grouped around a (001) plane in the parent orientation, resulting in three distinct groups of eight variants. When the same analysis as Figure 5 is done for Bain groups (see supplementary material), one Bain group

dominates in each case for PAG B, with 80% of the twin boundary region voxels, 65% connected and 93% overall. In PAG A, there is also a dominance of one Bain group at the boundary (60%) but when considering the whole grain, a different Bain group is dominant at 53%, having been just 13% in the twin boundary region. Finally, the individual variant proportions can be evaluated, as will be discussed later (see supplementary material for figures).

4 Discussion

In this paper, we have presented the results of a 3D EBSD tomography experiment in steel. The prior austenite grain microstructure was recovered using reconstruction codes in MTEX, on a slice by slice basis followed by slice to slice linking. This enabled a twinned internal grain to be identified. Following a further processing step, this grain was isolated and the variants analysed to look at variant selection, focussing on the twin boundary.

We propose the schematic at Figure 6 – note that the twin plane is split into a grain A and B pair, as per the schematic in Figure 4 (A). Figure 6 (A) shows the nucleation sites within the twin plane, where it is common to see twin related shared position and relative orientations. Two growth methods for the variants are then shown: Figure 6 (B) highlights in plane growth, which may self terminate or stop at another variant; and Figure 6 (C) covers out of plane growth, where this growth may terminate at the edge of the PAG grain or another variant. These are discussed in more detail in the following sections.

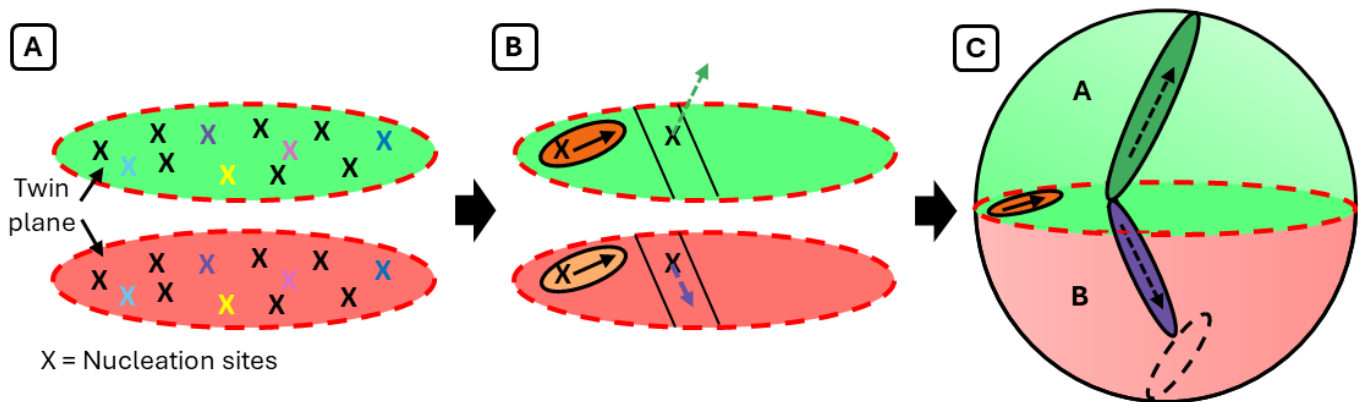


Figure 6 - Schematic showing how variants nucleate at the twin grain boundary. (A) nucleation sites in the twin planes – common colours indicate twin related nucleation (position & relative orientations); (B) In-plane nucleation and growth; (C) out-of-plane nucleation and growth.

4.1 In-plane growth

In the twin boundary thin layer, certain variants tend to grow within the plane. These variants are typically from the shared packet group and form a flat layer parallel to the twin boundary e.g. with the twin plane in the XY plane, growth is mainly restricted to this XY plane. Individual variants may self-terminate or stop at another variant (e.g. one that grows out of plane). As seen in Figure 5 (A), the shared packet accounts for ~50% of the voxels in the thin twin boundary region.

Figure 7 summarises data for shared packet variants at the twin boundary, including: an example of the variant growth (Figure 7 (A)), the relative proportions of the variants within the thin boundary region minimum misorientations between the variants within the shared packet (Figure 7 (C) and the orientations (Figure 7 (D)).

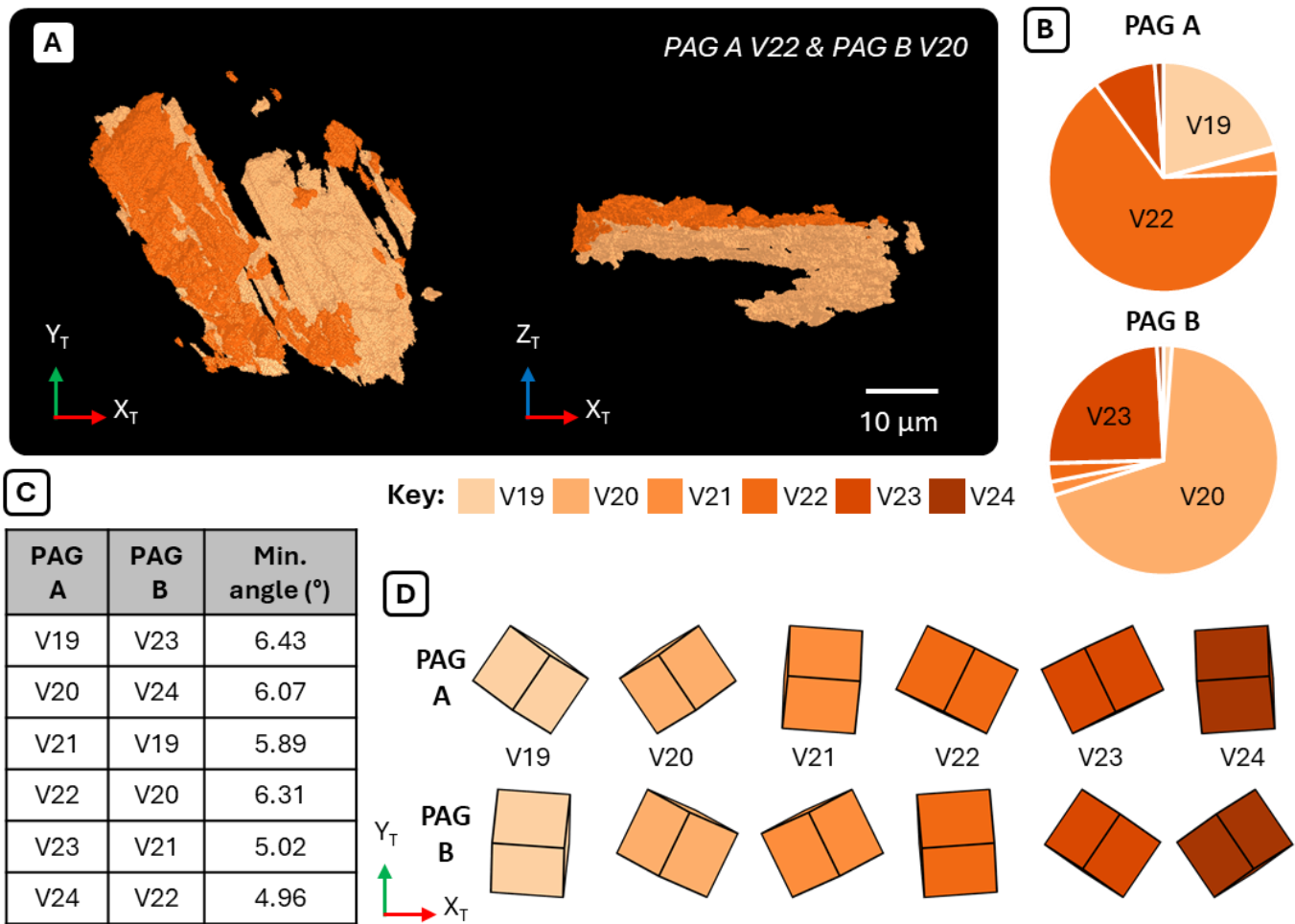


Figure 7 - Shared packet variants – in plane growth. (A) XY and XZ plane views for the largest variant in each PAG grain; (B) Distribution of the variants in the twin grain boundary region (2µm box) for each PAG grain; (C) Minimum misorientation angle between variants from each PAG and closest variant ID; (D) orientation cubes for the 6 variants in the shared packet group for each PAG.

Figure 7 (A) shows the largest shared packet variant (by volume) from each PAG, in both the XY and XZ planes. This data has not been restricted to the thin region at the twin boundary and shows the extent of the growth. These variants (PAG A V22 & PAG B V20) have a misorientation angle of 6.31°, which does give some potential for misidentification of voxels, but this does not seem to have a significant impact here, as the boundary between them is consistent with the twin boundary. The variant in PAG A is spatially co-located with parts of the variant in PAG B (which has a higher volume) and both variants appear to form wide, (mostly) flat laths across the twin region, the long axis of which corresponds to the $\langle 110 \rangle_{\gamma}$ in the PAG grains / $\langle 111 \rangle_{\alpha}$ in the variants. There are also gaps between the variants, where non-shared packet grains nucleate and grow.

The next largest variants for each PAG are also a pair, PAG A V19 & PAG B V23 (not shown), with a similar misorientation angle of 6.43° . In this case, the variants are restricted to a much thinner layer, with no out of plane growth. The variants are again spatially co-located, but this time mostly found at the edges of the layer, with some in plane growth at 60° to the pair in (Figure 7 (A)) seen. Overall, the same trend is seen, with sympathetic in plane growth, aligned with $\langle 110 \rangle_\gamma / \langle 111 \rangle_\alpha$, apparently either self terminated or terminated at other variants.

4.2 Out of plane growth

Moving to look at out of plane growth, we also see a relationship between the largest variants present in each PAG grain. This is best demonstrated by looking at one variant pair, as shown in Figure 8. Here, the largest isolated section (after connected component analysis in Dragonfly) of variant from the largest variant (by volume) for each PAG is shown. Figure 8 (A) shows the in plane view, with the region cut to just the thin section to look at how they relate at the twin grain boundary. Once again, we see spatial co-location and alignment (approx. $\langle 110 \rangle_\gamma / \langle 111 \rangle_\alpha$), with sympathetically related orientations for the variants.

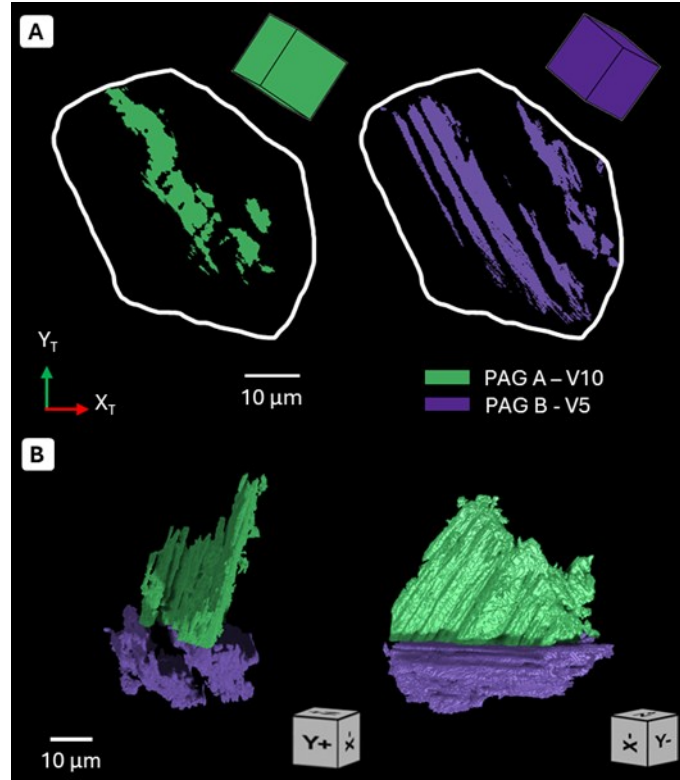


Figure 8 – Out of plane growth example. Largest isolated group of largest variant (by volume) for each PAG grain. (A) XY plane above and below the twin plane – a sketched outline is used for the twin plane outline; (B) 3D views

In Figure 8 (B), the variant pair is shown from two different angle, showing the different shapes of these variants in 3D. The reader is directed to the supplementary material for a video of this pair rotating through 360° , where the need to evaluate variants in 3D becomes far more apparent. The variant in PAG A resembles a thin triangular plane, whilst the variant in PAG A splits into 2 sections, neither of which is obvious from looking at a single direction (or 2D

cut). What can also be seen is the alignments of these variants with certain directions, which upon investigation align well with key directions in the PAG grains.

4.3 Twin boundaries and variant selection

Overall, this analysis reveals that the twin boundary has a strong impact on variant nucleation and growth, and variant selection. This is consistent with earlier 2D observations from low (0.04 wt%) and medium carbon (0.4 wt%) steels which suggested that the formation of annealing twins impacts bainite morphology by (i) blocking the growth of bainitic laths, (ii) providing potential nucleation sites for new laths [12,13] and (iii) impacting variant selection at the twins [3]. In the present work, by looking at a complete grain in 3D the influence of the PAG twins structure is clearer than a more limited 2D section-based analysis. For variants which have a high aspect ratio and specific shape with respect to each other, the 2D section-based analysis can render an individual variation contribution as a minor feature (e.g. reducing a rod-like variant to a small circular grain). The 3D analysis avoids this, as the volume can be analysed in full and a variety of 2D projections and 3D visualizations performed, in addition to the complete (volume-based) statistical analysis to explore location specific nucleation and growth.

The 3D data set here indicates that austenite twins can lead to variant selection and this is probably due to the fact that variant-variant combinations near a twin interface result in specific low & high angle grain boundaries between them (see [31]). For the final (i.e. room temperature) microstructure the nature of the grain orientations, and the grain boundaries, can strongly influence the properties of the final product. Well aligned slip systems, and specific populations of grain boundaries, can impact yield strength, work hardening, and the propagation of cleavage cracks. Further, impact toughness can also be affected [32], as there is evidence that the population of high angle grain boundaries and certain variant pairs have been shown to modify toughness as well as strength [2].

With knowledge of the impact of the twin boundary structure on variant selection, this now provides further opportunities to tailor the final microstructure by changing the number of annealing twins, for example, via small composition adjustments [33], or adjusting the thermomechanical processing route to increase the austenite grain size. Modification of the grain boundary population in FCC-materials is reasonably well explored, and the population of twins ($\Sigma 3$ boundaries) may be increased using grain boundary engineering [34]. Methods described in the literature include (i) increasing the grain size via extended grain growth where the density of annealing twins increases with grain size [33] leading to more $\Sigma 3$ boundaries [34,35], (ii) the use of iterative deformation and recrystallization steps [36] (for example, tailoring of the multi-step hot rolling process) or (iii) changing the stacking fault energy by alloying, e.g. in some steels, Ni increases and Mn decreases the stacking fault energy [37] where a decrease in stacking fault energy increases the probability of twin formation.

Ultimately In terms of the design of thermomechanical processing routes for steels, an exploration of the role of the twin-related variant structure could be valuable to influence critical materials properties.

Conclusions

We have carried out a tomography experiment on a linepipe steel to collect a 3D volume of EBSD data, 150 x 150 x 100 μm^3 with a 200 nm^3 voxel size. The high temperature austenite microstructure was reconstructed from the final microstructure, and this was used to isolate a complete, twinned, PAG grain within this volume. The twin grain boundary between the grains, and variants present in both grains was then evaluated in more detail, with the following conclusions:

- (1) Variants at the boundary are often spatially co-located and the larger variants have related orientations.
- (2) Some variants grow in-plane at the twin boundary – these are mostly the shared packet variants in this case.
- (3) Out of plane growth is often sympathetic, and variants may grow to the outer edge of the grain or be stopped by variants growing in from the grain boundary.
- (4) The twin boundary has a significant influence on the variants present within the PAG grain, as approximately half of the volume of the child variants (with respect to the entire PAG) are associated with the twin interface.

Analysis of variants within this grain demonstrates that high-temperature twin boundaries have a significant effect on variant selection and growth in the child microstructure. This suggests opportunities to engineer novel microstructures by controlling the high-temperature grain boundary character. Future work will assess the linkage between variant structure and the strength/toughness of high performance linepipe steels.

5 Author contributions

Ruth Birch: Writing – original draft, Writing – review & editing, Methodology, Investigation, Visualization. **Warren J. Poole:** Writing – review & editing, Supervision, Funding acquisition. **Ben Britton:** Writing – review & editing, Writing – original draft, Supervision, Funding acquisition.

6 Data Statement

The 3D dataset is available as raw h5oia files on Zenodo (DOI:10.5281/zenodo.18706015) and high quality figures and videos are available on figshare (DOI:10.6084/m9.figshare.31374256).

7 Funding

Electron microscopy was performed at the Electron Microscopy Laboratory (Materials Engineering, UBC), using the AMBER-X pFIB-SEM which was funded by the BCKDF and CFI-IF (39798: AM+). We acknowledge funding from an NSERC Alliance Grant (ALLRP 566973) with Interpro Pipe and Steel (formerly EVRAZ NA) and CFI Infrastructure

Operating Fund (38798) to support RB. Further, this work was undertaken in part, thanks to the funding from the Canada Research Chair program (WJP and TBB).

8 Acknowledgements

The authors would also like to express appreciation and to acknowledge the technical support from Interpro Pipe and Steel (formerly EVRAZ NA), in particular Dr. Michael Gaudet. The authors would like to thank Sabyasachi Roy for providing the sample and Professor Matthias Militzer for comments on the research.

This research was enabled in part by support provided by the Digital Research Alliance of Canada, formerly Compute Canada, and the Cedar cluster (now retired) located at Simon Fraser University.

9 References

- [1] H.K.D.H. Bhadeshia, Mechanism of the Bainite Transformation: A Turning Point, *Metall. Mater. Trans. A* 57A (2026) 1–20. <https://doi.org/10.1007/s11661-025-08017-7>.
- [2] Z.Q. Wang, Z.F. Guo, Y.S. Yu, C.J. Shang, R.D.K. Misra, Y.J. Hui, Understanding the Variant Pairing Effect on Yield Strength and Plasticity in Bainitic Steels, *Metall. Mater. Trans. A* 56 (2025) 3411–3416. <https://doi.org/10.1007/s11661-025-07788-3>.
- [3] M. Abbasi, T.W. Nelson, C.D. Sorensen, Analysis of variant selection in friction-stir-processed high-strength low-alloy steels, *J. Appl. Crystallogr.* 46 (2013) 716–725. <https://doi.org/10.1107/S0021889813008522>.
- [4] G. Miyamoto, N. Iwata, N. Takayama, T. Furuhashi, Mapping the parent austenite orientation reconstructed from the orientation of martensite by EBSD and its application to ausformed martensite, *Acta Mater.* 58 (2010) 6393–6403. <https://doi.org/10.1016/j.actamat.2010.08.001>.
- [5] D.A. Porter, K.E. Easterling, M.Y. Sherif, *Phase Transformations in Metals and Alloys* (3rd ed.), CRC Press, 2009. <https://doi.org/10.1201/9781439883570>.
- [6] Y. Mishiro, S. Nambu, J. Inoue, T. Koseki, Effect of Stress on Variant Selection in Lath Martensite in Low-carbon Steel, *ISIJ Int.* 53 (2013) 1453–1461. <https://doi.org/10.2355/isijinternational.53.1453>.
- [7] A. Mirzaei, R. Ghaderi, P.D. Hodgson, X. Ma, G.S. Rohrer, H. Beladi, The influence of parent austenite characteristics on the intervariant boundary network in a lath martensitic steel, *J. Mater. Sci.* 57 (2022) 8904–8923. <https://doi.org/10.1007/s10853-022-07204-w>.
- [8] A. Mirzaei, P.D. Hodgson, X. Ma, V.K. Peterson, E. Farabi, G.S. Rohrer, H. Beladi, The role of parent austenite grain size on the variant selection and intervariant boundary network in a lath martensitic steel, *Mater. Sci. Eng. A* 889 (2024) 145793. <https://doi.org/10.1016/j.msea.2023.145793>.
- [9] T. Furuhashi, H. Kawata, S. Morito, G. Miyamoto, T. Maki, Variant Selection in Grain Boundary Nucleation of

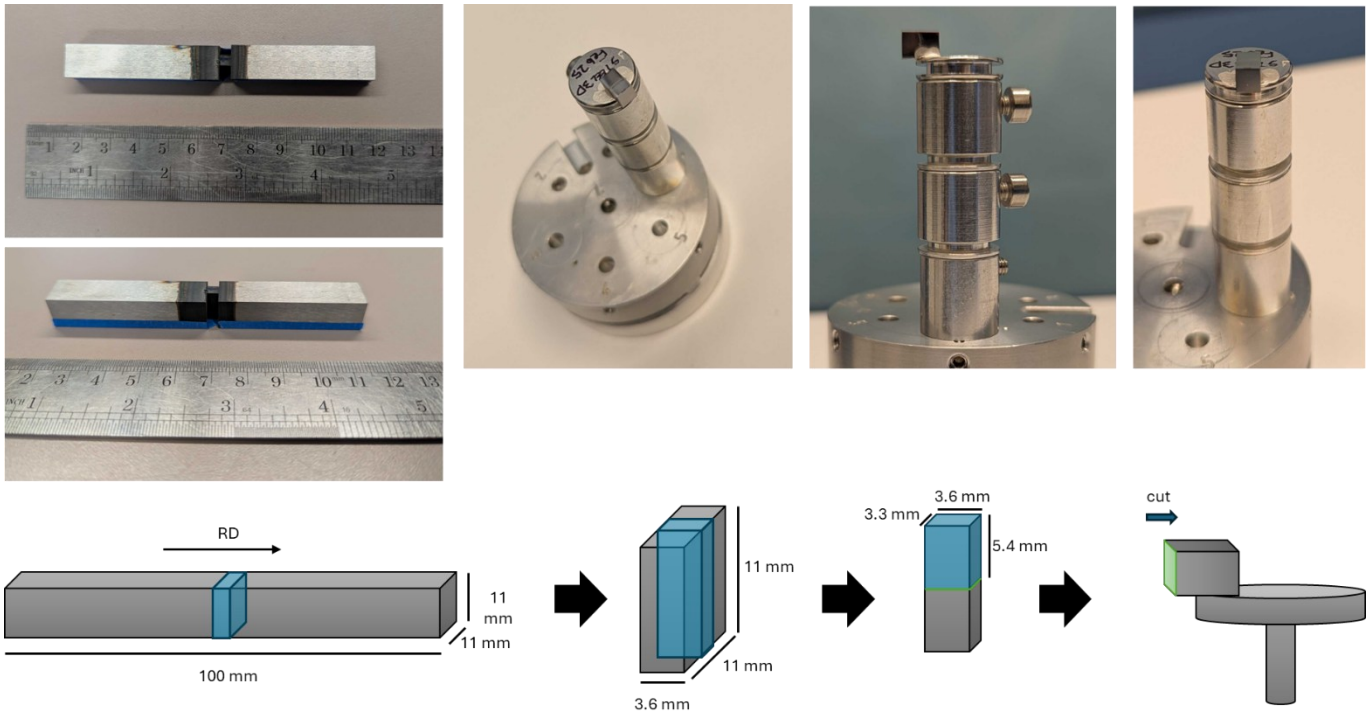
- Upper Bainite, *Metall. Mater. Trans. A* 39A (2008) 1003–1013. <https://doi.org/10.1007/s11661-008-9510-9>.
- [10] F. Lin, Y. Zhang, A. Godfrey, D. Juul Jensen, Twinning during recrystallization and its correlation with the deformation microstructure, *Scr. Mater.* 219 (2022) 114852. <https://doi.org/10.1016/j.scriptamat.2022.114852>.
- [11] S. Mahajan, Formation of annealing twins in f.c.c. crystals, *Acta Mater.* 45 (1997) 2633–2638. [https://doi.org/10.1016/S1359-6454\(96\)00336-9](https://doi.org/10.1016/S1359-6454(96)00336-9).
- [12] H. Hu, G. Xu, F. Liu, L. Wang, L. Zhou, Z. Xue, Dynamic observation of twin evolution during austenite grain growth in an Fe–C–Mn–Si alloy, *Int. J. Mater. Res.* 105 (2014) 337–341. <https://doi.org/10.3139/146.111037>.
- [13] H. Hu, B. Imed-Eddine, G. Xu, J. Tian, M. Zhou, Y. Bréchet, H.S. Zurob, Effect of temperature, carbon content and crystallography on the lengthening kinetics of bainitic ferrite laths, *Mater. Charact.* 187 (2022) 111860. <https://doi.org/10.1016/j.matchar.2022.111860>.
- [14] R.M. Birch, T. Ben Britton, W.J. Poole, Improving parent-austenite twinned grain reconstruction using electron backscatter diffraction in low carbon austenite, *Scr. Mater.* 257 (2025) 116459. <https://doi.org/10.1016/j.scriptamat.2024.116459>.
- [15] S. Zaefferer, S.I. Wright, D. Raabe, Three-dimensional orientation microscopy in a focused ion beam-scanning electron microscope: A new dimension of microstructure characterization, *Metall. Mater. Trans. A Phys. Metall. Mater. Sci.* 39 (2008) 374–389. <https://doi.org/10.1007/s11661-007-9418-9>.
- [16] G.D. West, R.C. Thomson, Combined EBSD/EDS tomography in a dual-beam FIB/FEG-SEM, *J. Microsc.* 233 (2009) 442–450. <https://doi.org/10.1111/j.1365-2818.2009.03138.x>.
- [17] J.J.L. Mulders, A.P. Day, Three-Dimensional Texture Analysis, *Mater. Sci. Forum* 495–497 (2005) 237–244. <https://doi.org/10.4028/www.scientific.net/msf.495-497.237>.
- [18] J. Guyon, N. Gey, D. Goran, S. Chalal, F. Pérez-Willard, Advancing FIB assisted 3D EBSD using a static sample setup, *Ultramicroscopy* 161 (2016) 161–167. <https://doi.org/10.1016/j.ultramic.2015.11.011>.
- [19] R. Birch, S. Li, S. Sharang, W.J. Poole, B. Britton, Large volume ‘ chunk ’ lift out for 3D tomographic analysis using analytical plasma focussed ion beam – scanning electron microscopy, *Micron* 203 (2026) 103986. <https://doi.org/10.1016/j.micron.2025.103986>.
- [20] A. Shibata, G. Miyamoto, S. Morito, A. Nakamura, T. Moronaga, H. Kitano, I. Gutierrez-Urrutia, T. Hara, K. Tsuzaki, Substructure and crystallography of lath martensite in as-quenched interstitial-free steel and low-carbon steel, *Acta Mater.* 246 (2023) 118675. <https://doi.org/10.1016/j.actamat.2023.118675>.
- [21] R.H. Petrov, O.L. García, N.S. Mouriño, L. Kestens, J.H. Bae, K.B. Kang, Microstructure - Texture Related Toughness Anisotropy of API-X80 Pipeline Steel Characterized by Means of 3D-EBSD Technique, *Mater. Sci.*

- Forum 558–559 (2007) 1429–1434. <https://doi.org/10.4028/www.scientific.net/MSF.558-559.1429>.
- [22] R.H. Petrov, O.L. García, J.J.L. Mulders, A.C.C. Reis, J.H. Bae, L. Kestens, Y. Houbaert, Three Dimensional Microstructure–Microtexture Characterization of Pipeline Steel, *Mater. Sci. Forum* 550 (2007) 625–630. <https://doi.org/10.4028/www.scientific.net/MSF.550.625>.
- [23] P.K. Parida, A. Dasgupta, D. Prasad, R. Mythili, S. Saibaba, Application of 3D EBSD Technique to Study Crystallographic Texture in Heavily Cold-Rolled and Recrystallized Modified 9Cr–1Mo Steel, *Trans. Indian Inst. Met.* 72 (2019) 663–672. <https://doi.org/10.1007/s12666-018-1517-3>.
- [24] M. Mosayebi, D. Paquet, P.-A. Deschênes, L. Tôn-Thât, B. Huang, N. Bassim, On the correlation between the habit plane and 3D morphology of lath martensite: A direct 3D observation using serial sectioning tomography of a low-carbon stainless steel, *Scr. Mater.* 255 (2025) 116367. <https://doi.org/10.1016/j.scriptamat.2024.116367>.
- [25] M. Mosayebi, P.A. Deschênes, D. Paquet, L. Tôn-Thât, N. Bassim, Three-dimensional analysis of local and dominant habit planes in a lath martensitic stainless steel, *Materialia* 42 (2025). <https://doi.org/10.1016/j.mtla.2025.102494>.
- [26] A. Shibata, G. Miyamoto, S. Morito, A. Nakamura, T. Moronaga, H. Kitano, I. Gutierrez-Urrutia, T. Hara, Three-dimensional crystallographic and local variant configuration analysis of lath martensite in medium-carbon steel, *Acta Mater.* 307 (2026) 121981. <https://doi.org/10.1016/j.actamat.2026.121981>.
- [27] M. Militzer, T. Garcin, W.J. Poole, In-situ measurements of grain growth and recrystallization by laser ultrasonics, *Mater. Sci. Forum* 753 (2013) 25–30. <https://doi.org/10.4028/www.scientific.net/MSF.753.25>.
- [28] F. Bachmann, R. Hielscher, H. Schaeben, Texture analysis with MTEX- Free and open source software toolbox, *Solid State Phenom.* 160 (2010) 63–68. <https://doi.org/10.4028/www.scientific.net/SSP.160.63>.
- [29] Comet Technologies Canada Inc. (Version 2025.1). Dragonfly 3D World. Available at <http://dragonfly.comet.tech/>, (2025).
- [30] T. Nyssönen, M. Isakov, P. Peura, V.-T. Kuokkala, Iterative Determination of the Orientation Relationship Between Austenite and Martensite from a Large Amount of Grain Pair Misorientations, *Metall. Mater. Trans. A* 47 (2016) 2587–2590. <https://doi.org/10.1007/s11661-016-3462-2>.
- [31] S. Morito, H. Tanaka, R. Konishi, T. Furuhashi, T. Maki, The morphology and crystallography of lath martensite in Fe-C alloys, *Acta Mater.* 51 (2003) 1789–1799. [https://doi.org/10.1016/S1359-6454\(02\)00577-3](https://doi.org/10.1016/S1359-6454(02)00577-3).
- [32] B.B. Wu, X.L. Wang, Z.Q. Wang, J.X. Zhao, Y.H. Jin, C.S. Wang, C.J. Shang, R.D.K. Misra, New insights from crystallography into the effect of refining prior austenite grain size on transformation phenomenon and consequent mechanical properties of ultra-high strength low alloy steel, *Mater. Sci. Eng. A* 745 (2019) 126–

136. <https://doi.org/10.1016/j.msea.2018.12.057>.
- [33] R.A. Varin, J. Kruszynska, Control of annealing twins in type 316 austenitic stainless steel, *Acta Metall.* 35 (1987) 1767–1774. [https://doi.org/10.1016/0001-6160\(87\)90122-2](https://doi.org/10.1016/0001-6160(87)90122-2).
- [34] S. Sinha, D.-I. Kim, E. Fleury, S. Suwas, Effect of grain boundary engineering on the microstructure and mechanical properties of copper containing austenitic stainless steel, *Mater. Sci. Eng. A* 626 (2015) 175–185. <https://doi.org/10.1016/j.msea.2014.11.053>.
- [35] P. Dolzhenko, M. Tikhonova, M. Odnobokova, R. Kaibyshev, A. Belyakov, On Grain Boundary Engineering for a 316L Austenitic Stainless Steel, *Metals (Basel)*. 12 (2022) 2185. <https://doi.org/10.3390/met12122185>.
- [36] H. Safari, A. Rezaeian, F. Karimzadeh, Novel role of thermomechanical grain boundary engineering in the microstructure evolution of austenitic stainless steel, *J. Mater. Res. Technol.* 30 (2024) 146–163. <https://doi.org/10.1016/j.jmrt.2024.03.056>.
- [37] V.M. Blinov, I.O. Bannykh, E.I. Lukin, O.A. Bannykh, E. V. Blinov, O.P. Chernogorova, M.A. Samoilova, Effect of Substitutional Alloying Elements on the Stacking Fault Energy in Austenitic Steels, *Russ. Metall.* 2021 (2021) 1325–1332. <https://doi.org/10.1134/S0036029521100086>.

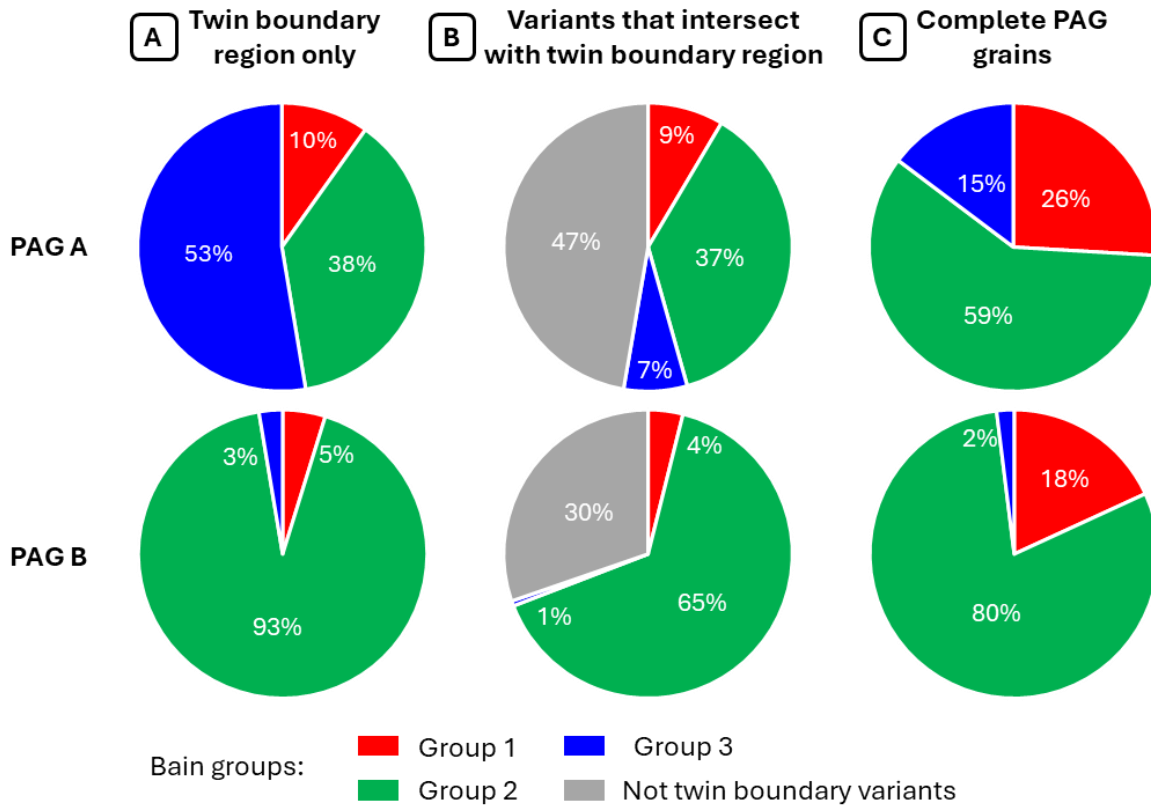
10 Supplementary Material

10.1 Sample Details

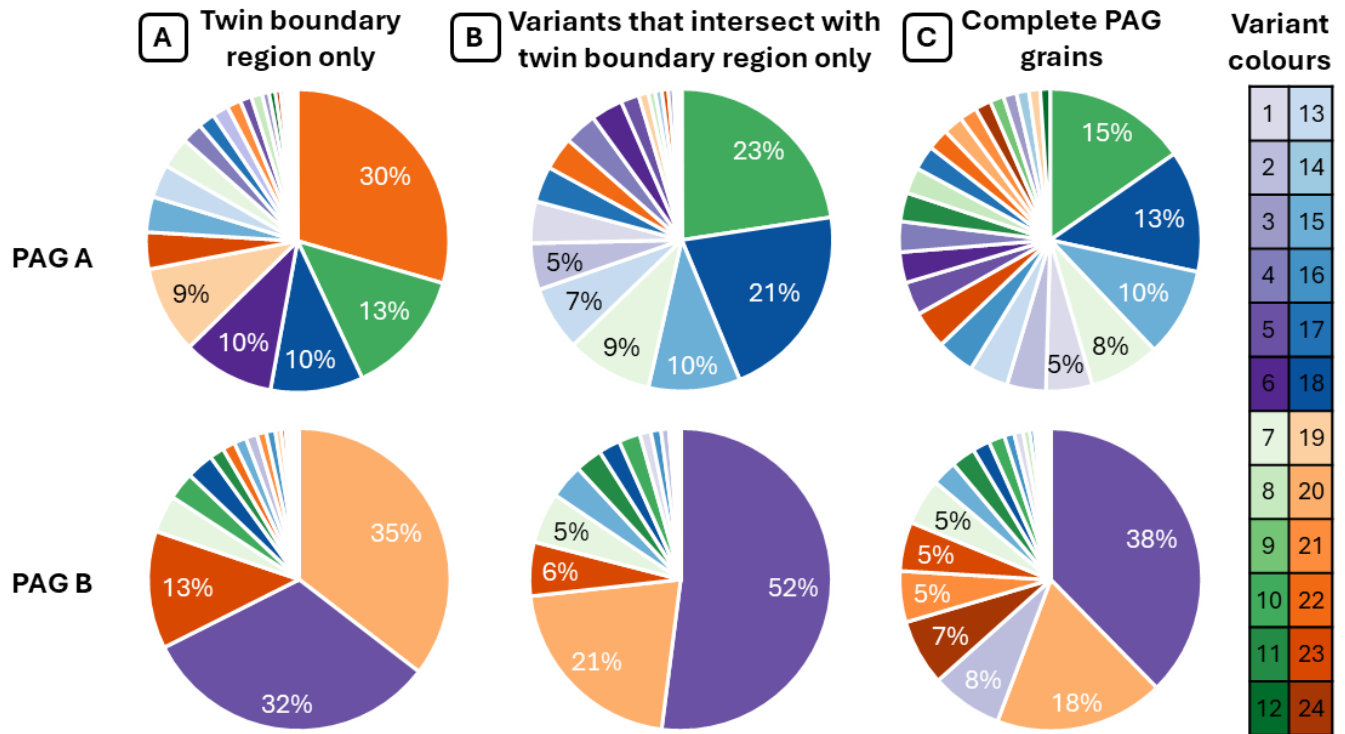


Sample details - Tomography cut relative to the sample for the heat treatment.

10.2 Variant composition – Bain groups



10.3 Variant composition – individual variants



Note: all segments $\geq 5\%$ are labelled

10.4 Videos and high quality images

Videos and high quality images for the figures in the paper are available at: DOI:10.6084/m9.figshare.31374256